Earth and Planetary Science Letters 562 (2021) 116849

Contents lists available at ScienceDirect

Earth and Planetary Science Letters

www.elsevier.com/locate/epsl

High-pressure experimental constraints of partitioning behavior of Si and S at the Mercury's inner core boundary

Renbiao Tao *, 1, Yingwei Fei

Earth and Planets Laboratory, Carnegie Institution for Science, 5251 Broad Branch Road, NW, Washington, DC 20015, USA

ARTICLE INFO

Article history:
Received 20 August 2020
Received in revised form 30 January 2021
Accepted 19 February 2021
Available online xxxx
Editor: J. Badro

Keywords:
Mercury's core
Fe-Si-S
partitioning
phase diagram
high-pressure

ABSTRACT

The partitioning of light elements between liquid and solid at the inner core boundary (ICB) governs compositional difference and density deficit between the outer and inner core. Observations of high S and low Fe concentration on the surface of Mercury from MESSENGER mission indicate that Mercury is formed under much more reduced conditions than other terrestrial planets, which may result in a Si and S-bearing metallic Fe core. In this study, we conducted high-pressure experiments to investigate the partitioning behavior of Si and S between liquid and solid in the Fe-Si-S system at 15 and 21 GPa, relevant to Mercury's ICB conditions. Experimental results show that almost all S partitions into liquid. The partitioning coefficient of Si (D_{Si}) between liquid and solid is strongly correlated with the S content in liquid (X_S^{liquid}) as: $\log_{10}(D_{Si}) = 0.0445 + 5.9895 * \log_{10}(1 - X_S^{liquid})$. Within our experimental range, pressure has limited effect on the partitioning behavior of Si and S between liquid and solid. For Mercury with an Fe-Si-S core, compositional difference between the inner and outer core is strongly dependent on the S content of the core. The lower S content is in the core, the smaller compositional difference and density deficit between the liquid outer core and solid inner core should be observed. For a core with 1.5 wt% bulk S, a model ICB temperature would intersect with the melting curve at ∼17 GPa, corresponding to an inner core with a radius of ∼1600 km.

1. Introduction

Model composition calculations show the Earth and other terrestrial planets contain silicate mantle and iron (Fe) dominant metallic cores (e.g., Morgan and Anders, 1980). Percolative core formation and silicate-metal differentiation naturally lead to incorporation of light elements, such as sulfur (S), silicon (Si), carbon (C) and oxygen (O), in the planetary core (Allégre et al., 1995; Kilburn and Wood, 1997; Poirier, 1994). Further, planetary cooling leads to solidification of any initially molten metallic core. The compositional difference and density deficit between liquid outer core and solid inner core must be governed by partitioning of light elements between liquid and solid iron at the inner core boundary (ICB) (Fei, 2017). Any compositional models of planetary core must produce consistent density and sound velocity profiles. In order to develop a planetary core composition model that meets geophysical constraints, it is also important to establish partitioning behavior for core materials (Fe and candidate light elements) between solid and liquid at high pressure and high temperature.

Mercury is the smallest, the closest to the Sun, and also the densest planet in our solar system (Anderson et al., 1987). It has been explored both by Earth-based telescope and by two NASA spacecraft missions: Mariner 10 (1974-1975) (Anderson et al., 1987) and MESSENGER (2008-2015) (Solomon and Byrne, 2019). MESSENGER spacecraft provided the opportunity to explore the Mercury's interior structure, consisting of a crust (∼50 km), mantle (∼260 km), and a big core (∼2030 km) with or without FeS "anticrust" (100 km?) (Cartier et al., 2020; Margot et al., 2012; McKinnon, 2012; Smith et al., 2012; Zuber et al., 2012). The most striking characteristic of the Mercury, besides its small size, is the relatively large mass fraction of core (65% of total mass), which contains a solid inner core and molten outer core (Charlier and Namur, 2019; Margot et al., 2012; Smith et al., 2010). Hauck et al. (2013) calculated several million modes of the radial density structure of Mercury using Monto Carlo techniques and estimated the top of the liquid Mercury's core at a radius of 2020 ± 30 km and the mean density of the Mercury's core at 6980 ± 280 kgm^{-3}. Geochemical data from MESSENGER have revealed details of Mercury's surface composition. For example, Mercurian surface is enriched in S (∼1-4 wt%) and C, and depleted in Fe, indicating that

---

* Corresponding author.
E-mail address: rbtao@pku.edu.cn (R. Tao).

[1] Present address: Center for High Pressure Science and Technology Advanced Research, Beijing 100094, China.

https://doi.org/10.1016/j.epsl.2021.116849
0012-821X/© 2021 Elsevier B.V. All rights reserved.

Mercury is formed under much more reduced conditions ($fO_2 =$ IW-4.5 $\sim$ IW-7.3) than other planet (Malavergne et al., 2010; McCubbin et al., 2012; Nittler and Weider, 2019; Zolotov et al., 2013). The extremely reducing condition during accretion and differentiation of Mercury have induced a large and partially molten core (Hauck and Johnson, 2019) and a substantial amount of Si could have be extracted and incorporated into the core-forming alloys (Cartier and Wood, 2019; Malavergne et al., 2010; McCubbin et al., 2012; Namur et al., 2016; Namur and Charlier, 2017; Nittler et al., 2011). Therefore, S and Si are considered as the most plausible light constituents in Mercury's core (Cartier and Wood, 2019; Malavergne et al., 2010).

High-pressure experimental technique is a powerful tool to study chemical and physical properties of planetary interior (Mao and Hemley, 2007). Large amounts of high-pressure experiments on the phase relation, equation-of-state, and sound velocities of relevant phases in Fe-S or Fe-Si binary system, under or approaching Earth's core conditions, have been extensively investigated (Li and Fei, 2014). Based on existing experimental partitioning data in the Fe-S systems, the S shows very large partition coefficient between liquid and solid of Fe alloy, which could result in large compositional difference and density deficit at planetary ICB (Buono and Walker, 2011; Chen et al., 2008; Fei et al., 2000, 1997). While in the Fe-Si binary system, phase relations at various pressure conditions showed Si has high solubility in iron and solubility of Si in solid iron increases with increasing pressure and temperature (Fischer et al., 2013). Meanwhile, partitioning coefficient of Si between liquid and solid below the eutectic composition is similar at $\sim$1 up to 145 GPa, indicating limited compositional difference (less than 2 wt%) and density deficit between inner and outer planetary core if Si is the predominant light element in the core (Fischer et al., 2013; Kuwayama and Hirose, 2004; Lin et al., 2002; Meco and Napolitano, 2005; Tateno et al., 2015). In spite of the importance of the effect of both S and Si on the physical properties of iron alloy, there is no study on the partitioning behavior of Si and S in the Fe-S-Si ternary system at Mercury's ICB conditions, although there were numbers of experimental studies aimed at understanding the behavior of elements under the strongly reduced condition of planetary interior in Fe-Si-S system at either lower pressure or much higher pressure than Mercury's ICB (Chabot et al., 2014; Kilburn and Wood, 1997; Morard et al., 2008; Morard and Katsura, 2010; Namur et al., 2016; Sanloup and Fei, 2004; Tateno et al., 2018). Ternary system experiments suggested that the interaction behaviors of light elements in the core system may be more complicated than ever thought before. A Fe-S and Fe-Si immiscibility liquid gap was observed at low pressure and it continuously shrinks with increasing pressure (Morard and Katsura, 2010; Sanloup and Fei, 2004), which implying that large portion of ternary Mercury's core is miscible and a potential composition valid for Mercury's core. On the other hand, chemical compositions of Fe-Si-S starting material for previous experiments are always higher than the eutectic composition, which is not consistent with real core situation with less light elements in outer liquid core than solid inner core.

In this study, we constrained high-pressure and high-temperature phase relations in the Fe-Si-S ternary system with S and Si concentration below eutectic composition at 15 and 21 GPa, relevant to Mercury's ICB conditions. The partitioning behaviors of Si and S between liquid and solid in the Fe-Si-S system at high pressure were also determined. Based on experimental results, we discussed distribution of Si and S, compositional difference and density deficit at the Mercury's ICB.

2. Experimental and analytical methods

2.1. Experimental procedure

All experiments were carried out in a 1500-ton multi-anvil device at the Geophysical Laboratory, Carnegie Institution for Science. The starting material was obtained by mixing Fe (99.9% purity, Alfa Aesar product), FeS (99.99% purity, Alfa Aesar product), and Fe-17wt.%Si (pre-alloy, Goodfellow product) powders. The chemical composition of the starting material is close to Fe $\sim$ 6wt.%S $\sim$ 4wt.%Si, which is below the eutectic composition in the Fe-Si-S system. The finely grounded starting material was loaded in an MgO capsule for each experiment (Fig. S-1). The 8/3 assembly, consisting of an MgO octahedron with a $LaCrO_3$ thermal insulator sleeve and a Re heater, was used for all experiments (Fig. S-1). The pressure was well calibrated using fixed phase transition points in $CaGeO_3$, SiO_2, and Mg_2SiO_4 (Bertka and Fei, 1997). The temperature was measured using a Type-C thermocouple, inserted axially to the top of the MgO capsule (Fig. S-1). The temperature gradient is less than 20 °C within the sample length ($<\sim$0.5 mm). Both pressure and temperature were automatically controlled through a computer program. The sample was first pressurized to desired pressure, then heated at a rate of 100 °C/min and held at a constant temperature for equilibrium (Table 1). Each experiment was quenched by shutting off the power, followed by automatic depressurization to ambient pressure at a rate of 1 GPa/hour.

Experiments were performed at pressures of 15 and 21 GPa and temperatures ranging from 800 °C to 1600 °C (Table 1). Although the equilibrium can be achieved within a couple of minutes in a liquid state for Fe-alloys (Kato and Ringwood, 1989), to well determine phase relationship and partitioning behavior in equilibrium, we carried out all experiments in tens of hours (Table 1). After experiments, recovered samples were mounted in epoxy resin, and polished with aluminum oxide powder ($<$1 μm) for measurements. The backscatter electron (BSE) images and chemical composition analysis for run products were obtained with a JEOL JXA-8530F Field Emission electron probe using standards (e.g. Fe metal, FeS_2, Fe_3O_4, and pyrope), a beam current of 30 nA and a 15-kV voltage with conventional ZAF data reduction techniques. Melt compositions were obtained by defocused 20 μm × 20 μm probe beam. The Mg ($<$0.1 wt%) and O ($<$0.8 wt%) contents in the Fe-alloy and melt were fairly low, indicating limited Mg and O from capsule was dissolved in samples (Table 2).

3. Results and discussion

3.1. High-pressure phase relations

At given pressure, a series of temperature-variable experiments were carried out to determine the phase relation in space of temperature (T) and composition (X). Melting texture was used to determine appearance of melting. The chemical compositions of liquid phases coexisting with solid phase at different temperatures were used to define the liquidus. At 15 GPa and 800 °C (LO1426), two solid phases (Fe-Si alloy and Fe_3S_2) were observed in run products, indicating that the temperature is below the solidus, and two solid phases are sub-solidus phases (Fig. S-2). At 900 °C (LO1455), melt was coexisted with two solid phases (Fig. 1a), indicating that the temperature is very closed to the solidus. The zonation of melt with two solid phases in LO1455 might be a consequence of the modest temperature gradient across the sample chamber (Fig. 1a). Considering melt phase in this run directly contacts with Fe-S solid instead of Fe-Si alloy (Fig. 1a), we expect the melt composition should represent the liquidus on the right side of eutectic point (Fig. 2a). The enriched S composition is likely resulted from the initial separation of the two sub-solidus phases,

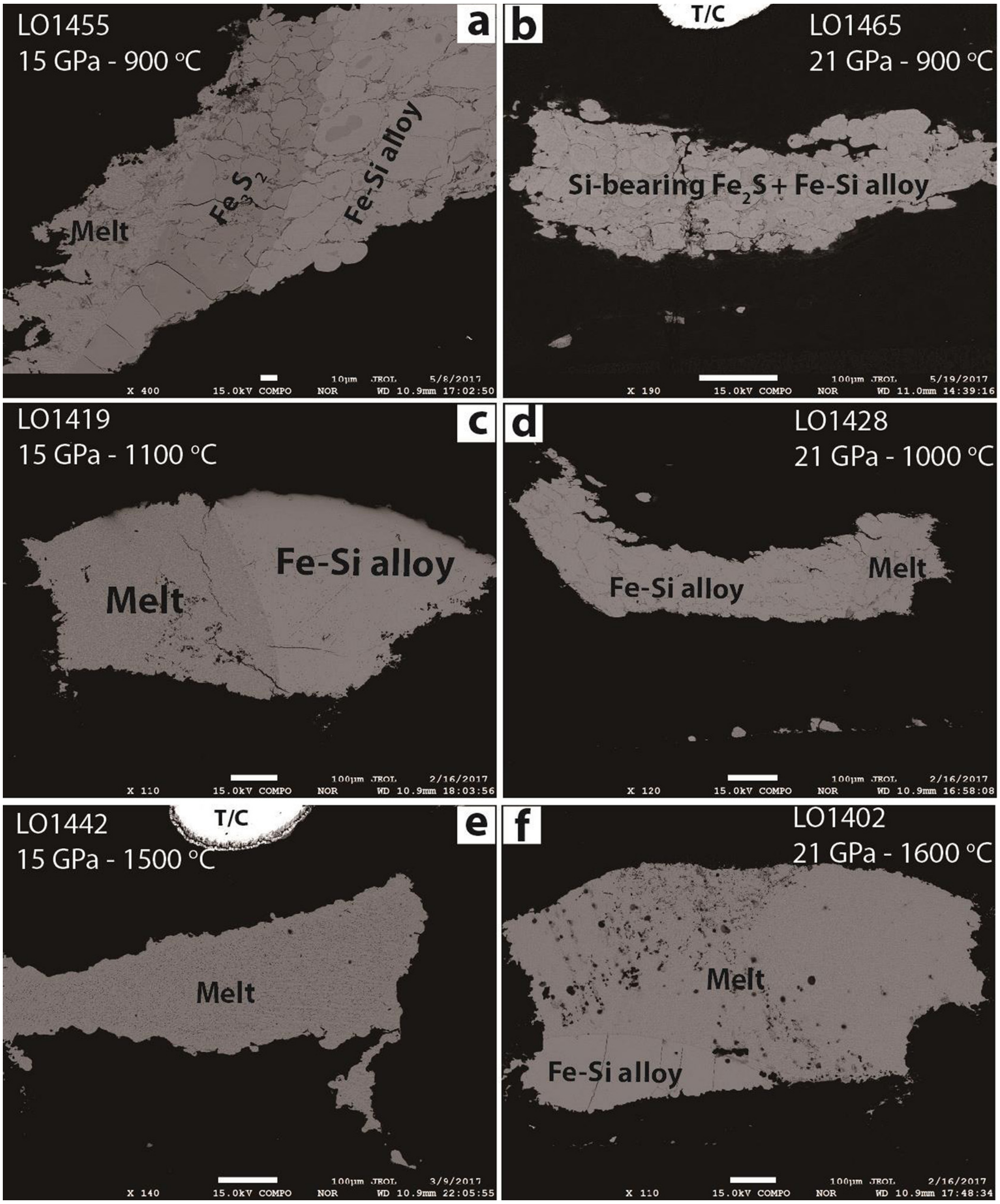

Fig. 1. Representative backscatter electron (BSE) images of run products at different pressure. (a, c, e) Experimental runs at 15 GPa from low to high temperature. (b, d, f) Experimental runs at 21 GPa from low to high temperature.

concentrated the Fe-Si alloy in one part of the capsule. At temperatures ranging from 1000 to 1400 °C (LO1441, LO1419, LO1427, LO1431, and LO1437), only one solid phase (Fe-Si alloy) is observed in equilibrium with melt (Table 1; Fig. S-2), indicating T-X conditions of these experiments are located between solidus and liquidus (e.g. Fig. 1c). At temperature above 1500 °C (LO1442), the sample was completely molten, indicating the temperature above liquidus at 15 GPa (Fig. 1e). At 21 GPa, similar phase transformations were observed from low to high temperature (Fig. 1b, d, and f; Fig. S-3), except that both solidus and liquidus are a slightly higher than those at 15 GPa. At 800 °C (LO1438) and 900 °C (LO1465), two sub-solidus phases (Fe-Si alloy and Fe-S solid) are observed (e.g. Fig. 1b; Fig. S-3). It is noted that the Fe content of the Fe-S solid is more consistent with $Fe_2(S,Si)$ instead of Fe_3S. From 1000 to 1600 °C (LO1428, LO1417, LO1414, LO1410, LO1404, and LO1402), melt is in equilibrium with one solid phase (Fe-Si alloy) (Fig. 1d and f; Table 1); Fig. S-3), indicating these experimental temperatures are between solidus and liquidus at 21 GPa.

Chemical compositions and calculated formulas for run products are listed in Table 2 and used to constrain the T-X phase relation in the Fe-Si-S system (Fig. 2). The melting temperatures of Fe-Si alloys with specific Si content without S (S = 0 wt%) at 15 and 21 GPa in this study are linearly interpolated from high-temperature phase diagram of Fe-Si system at room pressure (Meco and Napolitano, 2005) and at 21 GPa (Kuwayama and Hirose, 2004). At 15 GPa, two sub-solidus phases are formulated as Fe_3S_2 and Fe-Si alloy. Between solidus and liquidus, chemical compositions of solid and melt at different temperatures were used to define the T-X_S (S content in liquid) phase relation at 15 GPa (Fig. 2a). The S contents in solid Fe-Si alloys phase are normally lower than 0.1 wt%, indicating almost of all of S partition into liquid (Table 2). The S contents in melts generally decrease with

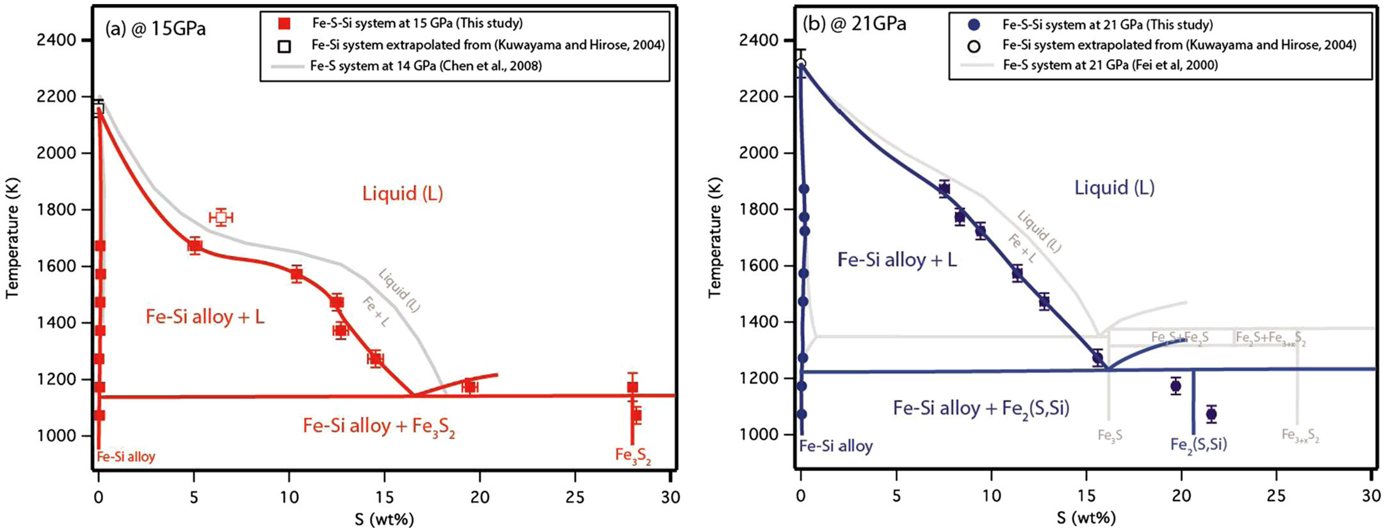

Fig. 2. Temperature (T)-composition (X_S, wt%) phase relations determined at different pressure. (a) T-X_S phase relation at 15 GPa in comparison with previous Fe-S phase relation at 14 GPa (Chen et al., 2008); (b) T-X_S phase relation at 21 GPa in comparison with previous Fe-S phase relation at 21 GPa (Fei et al., 2000).

increasing temperature. Less than 0.8 wt% and 0.2 wt% O were derived in melt and solid phase, respectively (Table 2). These minor O contents would not affect the interpretation necessarily. The chemical composition of melt phase above liquidus is Fe - 2.84 wt% Si-6.43 wt% S represent the chemical composition of starting material in this run. The solidus at 15 GPa is defined as a straight line at ∼900 °C in T-X_S phase diagram, while the liquidus is defined as a slope-changed curve with S content change (Fig. 2a). Similar slope change trend of liquidus in the Fe-S binary system at 14 GPa was observed in previous study (Chen et al., 2008), which is compared with that in this study (Gray curve in Fig. 2a). Chen et al. (2008) revealed this non-ideal liquidus curve at 14 GPa in Fe-S system and combined with existing data at lower pressure and above 20 GPa, they suggested a negative liquidus temperature gradient under conditions found at shallow depth in Mercury core. In comparison with liquidus in Fe-S binary system at 14 GPa (Chen et al., 2008), liquidus in the Fe-S-Si ternary system at 15 GPa in this study is generally about 50 °C lower due to Si effect.

Similarly, at 21 GPa, we also defined the T-X_S phase relation according to chemical compositions of run products (Fig. 2b). At 21 GPa, chemical compositions of sub-solidus phases are formulated as Fe-Si alloy and $Fe_2(S,Si)$ solid, which is different from that at 15 GPa. Up to 2.8 wt.% Si are also detected in $Fe_2(S,Si)$. The $Fe_2(S,Si)$ phase here replaces Fe_3S usually present at sub-solidus temperature in Fe-S system at 21 GPa (Fei et al., 2000). Limited S contents (<0.2 wt%) in solid Fe-Si alloy phases were also observed (Table 2). The S contents in the melts decrease with increasing temperature. The solidus at 21 GPa is defined as a straight line around 950 °C, while the liquidus was defined as quasi-ideal curve without obvious slope change (Fig. 2b). In compassion with the T-X_S phase relation in Fe-S binary system at same pressure (Fei et al., 2000), which was also plotted in Fig. 2b, several differences were observed. The Fe_3S, stable as sub-solidus high-pressure iron sulfide in the Fe-S binary system above 17 GPa, is not observed in the Fe-S-Si system at 21 GPa in this study, indicating that dissolved Si may have significantly effect on Fe-S phase stability. The stable sub-solidus phase is Si-bearing $Fe_2(S,Si)$, coexisting with Fe-Si alloy at 21 GPa. This could be of strong impact on Fe-Si-S core in Mercury, indicating the “FeS” layer at the core-mantle boundary may be $Fe_2(S,Si)$ instead of Fe_3S. On the other hand, both solidus and liquidus in the Fe-S-Si ternary system are about 50 °C lower than those in the Fe-S binary system at the same pressure and S content in liquids due to the effect of the Si content in the solid Fe-alloys on melting. For all experiments in this study, only one homogeneous liquid phase was observed at 15 GPa and 21 GPa, which is consistent with the expectations of earlier studies that reported immiscible melts only occur at low pressure (Chabot et al., 2014; Sanloup and Fei, 2004).

3.2. Partitioning of Si and S between solid and liquid

Fig. 3 shows the BSE image and EDS elemental (Fe, S and Si) maps of a typical run product (LO1419) with characteristic liquid quench texture. The EDS elemental map qualitatively showed the distribution of Fe (Fig. 3b), S (Fig. 3c), and Si (Fig. 3d) between liquid and solid. Almost all S partitions into liquid, while distribution of Si between liquid and solid varies at different experimental conditions. To quantitatively determine partitioning behavior of S and Si between liquid and solid, chemical compositions of all run products were analyzed with an electron microprobe (Table 2). We plotted chemical compositions (mol.%) of all run products and starting material in a ternary plot of Fe-S-Si system (Fig. 4). All solid Fe-Si alloys were plotted near the Fe corner in the ternary plot with variable Si and almost no S in them. With temperature decreasing, the S concentration in liquid (melt) phase increases until it reaches the eutectic composition (closed to the Fe_3S_2 composition) with very small amounts of Si (Fig. 4). Pressure has limited effect on chemical composition of melt and solid in our experimental pressure range.

On the basis of chemical compositions and calculated formulas of run products in Table 2, we know almost all S partitions into liquid if experimental PT condition is between solidus and liquidus. We fitted partitioning coefficient of Si (D_{Si}) between liquid and solid as a function of experimental P, T, and X_i (S and Si concentrations) in solid and liquid. The equilibrium reaction of Si between liquid and solid is described as chemical potential of Si between liquid and solid:

$$\mu(\mathrm{Si_{liquid}}) = \mu(\mathrm{Si_{solid}}) \tag{1}$$

The equilibrium constant (K) of the reaction can be written as:

$$\mathrm{K} = (\gamma_{\mathrm{Si}}^{\mathrm{solid}} * \mathrm{X}_{\mathrm{Si}}^{\mathrm{solid}})/(\gamma_{\mathrm{Si}}^{\mathrm{liquid}} * \mathrm{X}_{\mathrm{Si}}^{\mathrm{liquid}}) \tag{2}$$

where $\gamma_{\mathrm{Si}}^{\mathrm{liquid}}$ and $\gamma_{\mathrm{Si}}^{\mathrm{solid}}$ are the activity coefficient of Si components in liquid and solid, respectively. $\mathrm{X}_{\mathrm{Si}}^{\mathrm{liquid}}$ and $\mathrm{X}_{\mathrm{Si}}^{\mathrm{solid}}$ are the mole fraction of Si components in liquid and solid, respectively.

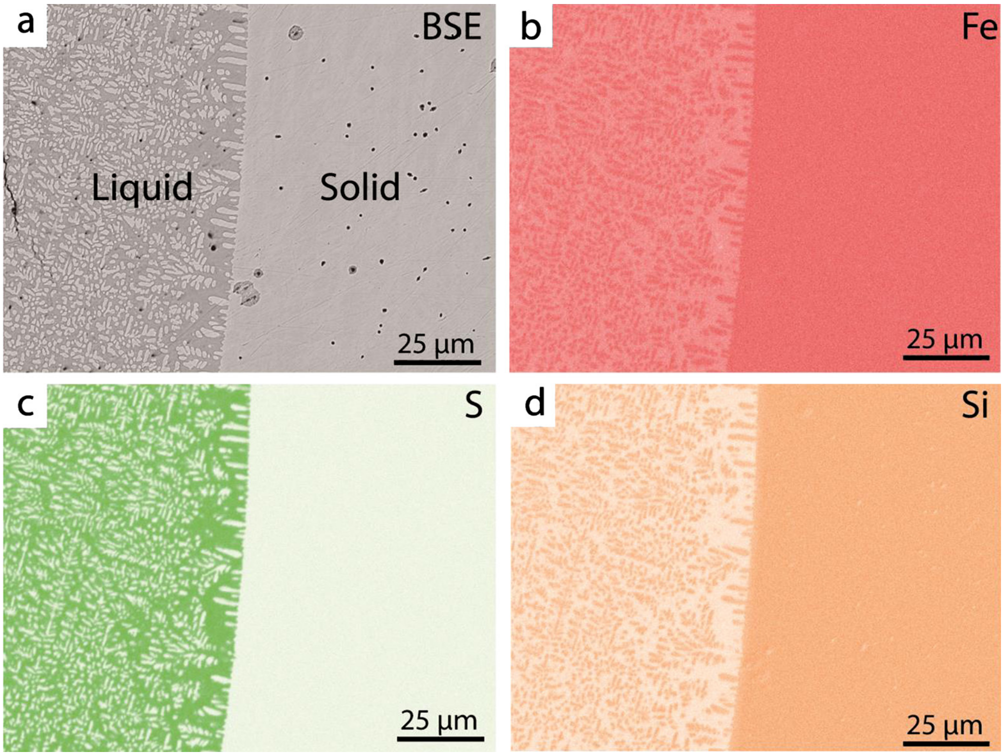

Fig. 3. Representative BSE image and EDS elemental (Fe, S, Si) maps at boundary between solid and liquid phases in run product. The texture and element distribution were quenched from 15 GPa and 1100 °C (LO1419).

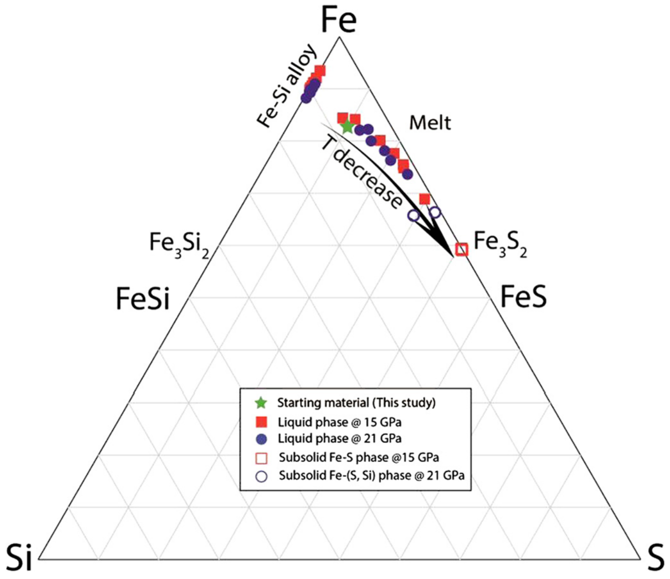

Fig. 4. Chemical compositions of all run products in ternary plot of Fe-S-Si system (mole ratio). Melt compositions evolve from starting material (green star) to the S content close to Fe_3S_2 with decreasing temperature. (For interpretation of the colors in the figure(s), the reader is referred to the web version of this article.)

Therefore, the partitioning coefficient of Si between liquid and solid can be defined as:

$$D_{Si} = X_{Si}^{liquid}/X_{Si}^{solid} = K * (\gamma_{Si}^{solid}/\gamma_{Si}^{liquid}) \qquad (3)$$

If limited effect of pressure on the γ_{Si}^{liquid} and γ_{Si}^{solid} was reasonably assumed in our experimental range, following previous approaches (Wade and Wood, 2005), D_{Si} can be parameterized as follows:

$$\log_{10}(D_{Si}) = a + b/T + cP/T + d\log_{10}(1 - X_S^{liquid}) + e\log_{10}(1 - X_{Si}^{liquid}) + f\log_{10}(1 - X_{Si}^{solid}) \qquad (4)$$

where T is temperature in kelvin and P is pressure in GPa, X_S^{liquid}, X_{Si}^{liquid}, X_{Si}^{solid} are the mole fraction of S and Si in liquid and solid, respectively. The partitioning of Si between liquid and solid calculated from the T-X_{Si} phase relation of Fe-Si binary system at 21 GPa in previous study (Kuwayama and Hirose, 2004) was also used to parameterize the partitioning coefficient of Si in equation (4). Parameters a, b, c, d, e, f are determined using a weighted linear least-squares fit. From the T-X_S phase relation in Fig. 2a and b, we have shown that the S content in the liquid (X_S) is temperature-dependent. The higher temperature, the lower S contents in liquid. They are correlated parameters, so only one of them was chosen to fit equation (4). A fit of experimental data shows d is the only correlated parameter while b, c, e, and f are not statistically significant. The linearly corrected relation between $\log_{10}(D_{Si})$ and $\log_{10}(1 - X_S^{liquid})$ is plotted in Fig. 5a as:

$$\log_{10}(D_{Si}) = 0.0445(\pm 0.025) + 5.9895(\pm 0.283) \times \log_{10}(1 - X_S^{liquid}) \qquad (5)$$

with $R^2 = 0.98$.

The zero value for parameters b, c, e, and f indicates limited effect of pressure, temperature, and Si concentration in liquid on Si partitioning behavior between liquid and solid in our experimental P-T range. The partitioning of Si between liquid and solid is only compositionally dependent on X_S^{liquid}. The calculated D_{Si} from equation (5) and the experimentally measured D_{Si} from this study and previous study (Kuwayama and Hirose, 2004) plot on the 1:1 line (Fig. S-4), indicating an excellent representation of the experimental data by the model.

Alternatively, we can also fit the data with a linear relationship between $\log_{10}(D_{Si})$ and 1/T, as shown in Fig. 5b.

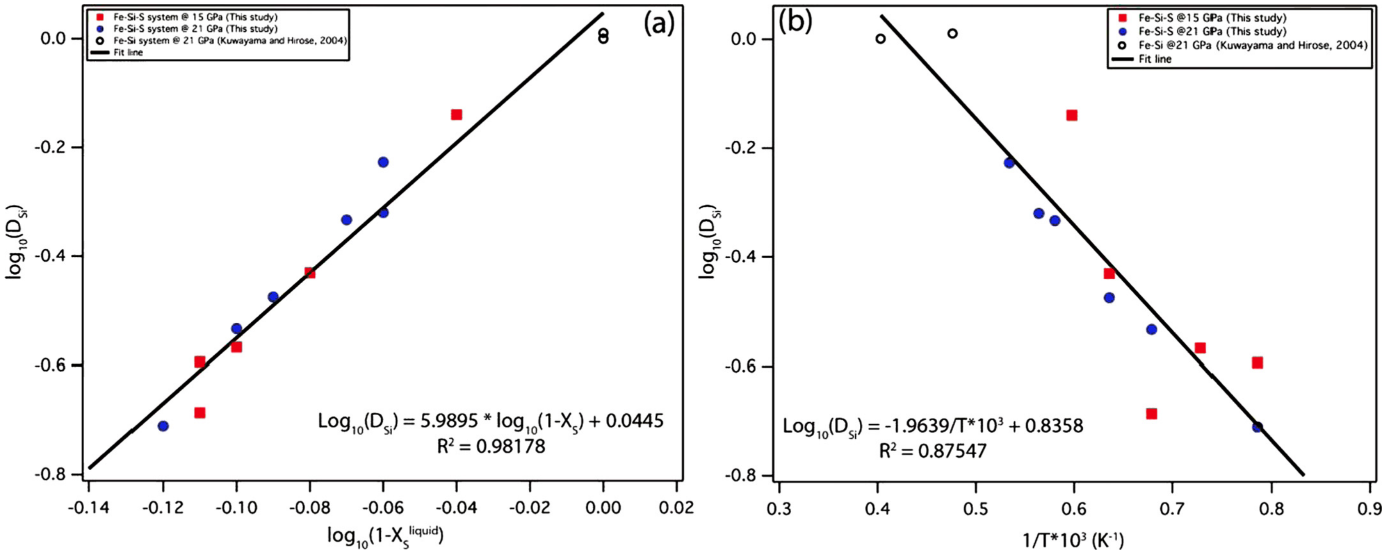

Fig. 5. (a) Partitioning of Si between liquid and solid [$\log_{10}(D_{Si})$] is linearly correlated with [$\log_{10}(1 - X_S^{liquid})$]. (b) Partitioning of Si between liquid and solid [$\log_{10}(D_{Si})$] changes linearly with 1/T.

$$\log_{10}(D_{Si}) = 1.9639(\pm 0.087)/T \times 10^3 + 0.8358(\pm 0.035) \qquad (6)$$

with $R^2 = 0.88$.

The correlation between $\log_{10}(D_{Si})$ and 1/T is not as good as that between $\log_{10}(D_{Si})$ and $\log_{10}(1 - X_S^{liquid})$ (cf. Fig. 5a and 5b). In Fig. 5b, all experimental data at 21 GPa are much better represented by equation (6) whereas the data at 15 GPa have a large deviation. This may be due to non-ideal liquidus curve at lower pressure in the Fe-S system. For two experimental points (open circle) at 21 GPa from (Kuwayama and Hirose, 2004) in Fig. 5b, in their temperature range, the D_{Si} below eutectic composition are stable at ~1. This indicated, for a S-free Fe-Si system, partitioning of Si between liquid and solid below eutectic composition are not T dependent. When the S is introduced in Fe-Si system, the partitioning of Si between liquid and solid will be correlated with S concentration in the system (Fig. 5a).

4. Implications for Mercury's core

Four key events in the origin hypothesis of Mercury have been proposed (Cartier and Wood, 2019; Charlier and Namur, 2019): (A) Global melting of the planet and separation of a metallic core from a silicate magma ocean; (B) Cooling of the planet, progressive crystallization of the solid inner core and crystallization of magma ocean to produce primordial mantle; (C) Partial melting of the mantle, production of the secondary crust, and synchronous cratering of the surface; (D) Termination of major volcanism. During Mercury's cooling, solidification of initially molten metallic core would have resulted in re-partitioning of S and Si between liquid and solid at the inner core boundary (ICB), which governs the compositional difference and density deficit between the outer and inner core.

4.1. Pressure estimated at Mercury's ICB

The liquidus temperatures of Fe-Si-S system at 15 GPa and 21 GPa are constrained at ~1950 K and ~2300 K in Fig. 3 in this study, respectively, if 1.5 wt% bulk S in Mercury's core was assumed (Namur et al., 2016). Consistently, the liquids temperature range from 1950 at 15 GPa to 2300 K at 21 GPa covers recent estimated ICB temperature at ~2050 K for Mercury's from thermal modeling (Knibbe and van Westrenen, 2018). If the ICB temperature of Mercury's core crosses the melting of this model Fe-Si-S composition, then the possible ICB pressure of Mercury can be estimated at ~17 GPa, corresponding a solid inner core with a radius of ~1600 km. A smaller inner core would require an increase of the temperature or S content of Mercury's core.

4.2. Partitioning S and Si between silicate and Fe metal during Mercury's core formation

Chabot et al. (2014) experimentally constrained the partitioning behaviors of Si and S between silicate melts and molten Fe metal at room pressure and high-temperature and found that metallic melts with a range of S and Si combinations can be in equilibrium with silicate melt with S contents consistent with Mercurian surface, indicating Mercury's core likely contains Si and S. Kilburn and Wood (1997) determined the partitioning of a number of siderophile and lithophile elements between liquid metal and liquid silicate phase at high temperature and 2.5 GPa and found that Si and S are incompatible during a single-stage low-pressure core formation event. As oxygen fugacity is reduced, Si becomes increasingly siderophile and S increasingly lithophile. Namur et al. (2016) also performed experiments at high temperature (1200-1750 °C) and pressures from 1 bar to 4 GPa under highly reduced condition (IW-1.5 to IW-9.4) on compositions representative of Mercurian lavas and on the silicate composition of an enstatite chondrite, and found that S concentration in silicate melts at sulfide saturation increases with increasing reducing conditions and with temperature. During experiments, metallic melts have a low S content which decreases from 3 wt.% at IW-2 to 0 wt.% at IW-9, and an oxygen fugacity at Mercury's interior at IW-5.4 ± 0.4 was suggested based on S contents on Mercury's surface (Namur et al., 2016). These experimental results provided some constraints on the bulk S and Si that could be incorporated into the core during differentiation. The planet cooling could lead to further redistribution of S and Si between solid inner core and liquid outer core.

4.3. Compositional difference at Mercury's ICB

In this study, we constrained the partitioning of Si and S between liquid and solid in the Fe-Si-S system at 15 and 21 GPa, relevant to Mercury's ICB conditions. Experimental results show that partitioning of Si is linearly dependent on S content in liquid (Equation (5)), and almost all S partitions into liquid outer core. For a Mercury's Fe-S-Si core, if there is no S in the Mercury core, the partitioning of Si (D_{Si}) is at near ~1, indicating liquid outer core and solid inner core have similar Si concentration. In this case, there will be not significant compositional difference and density deficit at Mercury's ICB. If the X_S in the Mercury's core is greater than ~30 mole %, then the D_{Si} will be calculated at ~0 according to equation (5), indicating all S partition in liquid outer core and most of Si will partition into solid inner core. In this case, the compositional difference and density deficit at Mercury's ICB will be the largest. Therefore, the compositional difference and density deficit at Mercury's ICB is strongly dependent on the S content.

Namur et al. (2016) experimentally studied the effect of oxygen fugacity on the S solubility in mafic melt and discussed the speciation and distribution of S on the Mercury. Based on the assumption of bulk Mercury's S content (~4 wt.%) (Nittler et al., 2011), they constrained the oxygen fugacity of Mercury's interior to IW-5.4, and S content in Mercury's mantle at 7-11 w%, and S content in metallic core below 1.5 wt%. Chabot et al. (2014) conducted a set of equilibrium metal-silicate experiments and determined the effect of metallic composition in Fe-S-Si system on the S concentration in the coexisting silicate melt. They found the metal-silicate S partitioning coefficient, D_S, is linearly correlated with the Si content of the metal: $\text{Log}[D_S] = 1.35 - 0.15 * [\text{wt\% Si}_{\text{metal}}]$ (Chabot et al., 2014). Therefore, combining the estimated S contents in mantle and core (Namur et al., 2016) and the correlation between D_S and Si content in metal (Chabot et al., 2014), the Si content in the Mercury's bulk core is estimated in the range of 13.5 −14.8 wt%. If the S content in bulk core of Mercury (<1.5 wt%) (Namur et al., 2016) is taken, then the partitioning of Si [D_{Si}] between liquid outer core and solid inner core would be constrained above 0.96 according to equation (5). In this scenario, all S (<1.5%) would partition into the liquid outer core, whereas the Si concentration between the inner and outer core would be almost the same, indicating a limited compositional difference and density deficit at Mercury's ICB. This assumes that the Si partitioning of this study at low Si concentration is applicable to the inferred Si content in Mercury's core at ~14 wt%. Further study of Si-rich and S-poor core composition, combined with phase stability of Si-rich Fe-Si alloys at inner-core conditions, is needed.

A more interesting case is if Mercury's core contains moderate or high S content. With increasing the S content, Si is preferentially partitioning into the solid core and S remains in the liquid outer core. The high S content also drives down the melting temperature, leading to a smaller inner core for the same core temperature profile. Our experimental melting and partitioning data provide quantitative constraints on the tradeoff among model parameters such as the light element ratio, inner core size, and thermal structure, and density contrast between the inner and outer core.

5. Conclusions

In this study, we experimentally determined the partitioning behavior of Si and S between liquid and solid in the Fe-Si-S system at 15 and 21 GPa. The experimental results showed almost all the S partitions into liquid, while the partitioning of Si between liquid and solid is linearly correlated with S content in the liquid. We applied our experimental result to Mercury's core and modeled the possible compositional distribution between Mercury's inner and outer core. Finally, we drew following conclusions for Mercury's core:

1. A Si-rich solid inner core and a S-rich liquid outer core for Mercury are suggested.
2. For a Mercury's core with 1.5 wt% bulk S, a model ICB temperature of ~2050 K would cross the melting at ~17 GPa, corresponding a solid inner core with a radius of ~1600 km.
3. The bulk S content in Mercury's core is the dominant factor to determine the compositional difference and density deficit at Mercury's ICB. The S content is correlated positively to the density deficit and negatively to the size of the inner core.

CRediT authorship contribution statement

Renbiao Tao and Yingwei Fei: Conceptualization. **Renbiao Tao:** Carrying out experiments, Data curation, Writing – Original draft preparation. **Yingwei Fei:** Supervision. **Renbiao Tao and Yingwei Fei:** Writing – Reviewing and Editing.

Declaration of competing interest

The authors declare that they have no known competing financial interests or personal relationships that could have appeared to influence the work reported in this paper.

Acknowledgement

This work was supported by the National Science Foundation (grants EAR-1447311 and EAR-1619868 to Y.F.). We thank Asmaa Boujibar and Zhixue Du for helpful discussions. We also thank three anonymous reviewers and editor James Badro for their constructive comments and suggestions.

Appendix A. Supplementary material

Supplementary material related to this article can be found online at https://doi.org/10.1016/j.epsl.2021.116849.

References

Allégre, C.J., Poirier, J.-P., Humler, E., Hofmann, A.W., 1995. The chemical composition of the Earth. Earth Planet. Sci. Lett. 134, 515–526.

Anderson, J.D., Colombo, G., Esposito, P.B., Lau, E.L., Trager, G.B., 1987. The mass, gravity field, and ephemeris of Mercury. Icarus 71, 337–349. https://doi.org/10.1016/0019-1035(87)90033-9.

Bertka, C.M., Fei, Y., 1997. Mineralogy of the Martian interior up to core-mantle boundary pressure. J. Geophys. Res. 102, 5251–5264. https://doi.org/10.1029/96JB03270.

Buono, A.S., Walker, D., 2011. The Fe-rich liquidus in the Fe–FeS system from 1 bar to 10 GPa. Geochim. Cosmochim. Acta 75, 2072–2087. https://doi.org/10.1016/j.gca.2011.01.030.

Cartier, C., Namur, O., Nittler, L.R., Weider, S.Z., Crapster-Pregont, E., Vorburger, A., Frank, E.A., Charlier, B., 2020. No FeS layer in Mercury? Evidence from Ti/Al measured by MESSENGER. Earth Planet. Sci. Lett. 534, 116108. https://doi.org/10.1016/j.epsl.2020.116108.

Cartier, C., Wood, B.J., 2019. The role of reducing conditions in building Mercury. Elements 15, 39–45. https://doi.org/10.2138/gselements.15.1.39.

Chabot, N.L., Wollack, E.A., Klima, R.L., Minitti, M.E., 2014. Experimental constraints on Mercury's core composition. Earth Planet. Sci. Lett. 390, 199–208. https://doi.org/10.1016/j.epsl.2014.01.004.

Charlier, B., Namur, O., 2019. The origin and differentiation of planet Mercury. Elements 15, 9–14. https://doi.org/10.2138/gselements.15.1.9.

Chen, B., Li, J., Hauck, S.A., 2008. Non-ideal liquidus curve in the Fe-S system and Mercury's snowing core. Geophys. Res. Lett. 35, L07201. https://doi.org/10.1029/2008GL033311.

Fei, Y., 2017. Constraints on the light elements in the core from partitioning and mineral physics data. In: Goldschmidt2017 Abstract. Presented at the Goldschmidt, p. 1125.

Fei, Y., Bertka, C.M., Finger, L.W., 1997. High-pressure iron-sulfur compound, Fe_3S_2, and melting relations in the Fe-FeS system. Science 275, 1621–1623. https://doi.org/10.1126/science.275.5306.1621.

Fei, Y., Li, J., Bertka, C.M., Prewitt, C.T., 2000. Structure type and bulk modulus of Fe_3S, a new iron-sulfur compound. Am. Mineral. 85, 1830–1833. https://doi.org/10.2138/am-2000-11-1229.

Fischer, R.A., Campbell, A.J., Reaman, D.M., Miller, N.A., Heinz, D.L., Dera, P., Prakapenka, V.B., 2013. Phase relations in the Fe–FeSi system at high pressures and temperatures. Earth Planet. Sci. Lett. 373, 54–64. https://doi.org/10.1016/j.epsl.2013.04.035.

Hauck, S.A., Johnson, C.L., 2019. Mercury: inside the iron planet. Elements 15, 21–26. https://doi.org/10.2138/gselements.15.1.21.

Hauck, S.A., Margot, J.-L., Solomon, S.C., Phillips, R.J., Johnson, C.L., Lemoine, F.G., Mazarico, E., McCoy, T.J., Padovan, S., Peale, S.J., Perry, M.E., Smith, D.E., Zuber, M.T., 2013. The curious case of Mercury's internal structure. J. Geophys. Res., Planets 118, 1204–1220. https://doi.org/10.1002/jgre.20091.

Kato, T., Ringwood, A.E., 1989. Melting relationships in the system Fe-Feo at high pressures: implications for the composition and formation of the Earth's core. Phys. Chem. Miner. 16, 524–538. https://doi.org/10.1007/BF00202207.

Kilburn, M.R., Wood, B.J., 1997. Metal–silicate partitioning and the incompatibility of S and Si during core formation. Earth Planet. Sci. Lett. 152, 139–148. https://doi.org/10.1016/S0012-821X(97)00125-8.

Knibbe, J.S., van Westrenen, W., 2018. The thermal evolution of Mercury's Fe–Si core. Earth Planet. Sci. Lett. 482, 147–159. https://doi.org/10.1016/j.epsl.2017.11.006.

Kuwayama, Y., Hirose, K., 2004. Phase relations in the system Fe-FeSi at 21 GPa. Am. Mineral. 89, 273–276. https://doi.org/10.2138/am-2004-2-303.

Li, J., Fei, Y., 2014. Experimental constraints on core composition. In: Treatise on Geochemistry, Vol. 3, 2nd edition, pp. 527–557.

Lin, J.-F., Heinz, D.L., Campbell, A.J., Devine, J.M., Shen, G., 2002. Iron-silicon alloy in Earth's core? Science 295, 313–315. https://doi.org/10.1126/science.1066932.

Malavergne, V., Toplis, M.J., Berthet, S., Jones, J., 2010. Highly reducing conditions during core formation on Mercury: implications for internal structure and the origin of a magnetic field. Icarus 206, 199–209. https://doi.org/10.1016/j.icarus.2009.09.001.

Mao, H.-k., Hemley, R.J., 2007. The high-pressure dimension in Earth and planetary science. Proc. Natl. Acad. Sci. 104, 9114–9115. https://doi.org/10.1073/pnas.0703653104.

Margot, J.-L., Peale, S.J., Solomon, S.C., Hauck, S.A., Ghigo, F.D., Jurgens, R.F., Yseboodt, M., Giorgini, J.D., Padovan, S., Campbell, D.B., 2012. Mercury's moment of inertia from spin and gravity data. J. Geophys. Res. 117, E00L09. https://doi.org/10.1029/2012JE004161.

McCubbin, F.M., Riner, M.A., Vander Kaaden, K.E., Burkemper, L.K., 2012. Is Mercury a volatile-rich planet? Geophys. Res. Lett. 39, L09202. https://doi.org/10.1029/2012GL051711.

McKinnon, W.B., 2012. The strangest terrestrial planet. Science 336, 162–163. https://doi.org/10.1126/science.1220825.

Meco, H., Napolitano, R.E., 2005. Liquidus and solidus boundaries in the vicinity of order–disorder transitions in the Fe–Si system. Scr. Mater. 52, 221–226. https://doi.org/10.1016/j.scriptamat.2004.09.026.

Morard, G., Katsura, T., 2010. Pressure–temperature cartography of Fe–S–Si immiscible system. Geochim. Cosmochim. Acta 74, 3659–3667. https://doi.org/10.1016/j.gca.2010.03.025.

Morard, G., Sanloup, C., Guillot, B., Fiquet, G., Mezouar, M., Perrillat, J.P., Garbarino, G., Mibe, K., Komabayashi, T., Funakoshi, K., 2008. In situ structural investigation of Fe-S-Si immiscible liquid system and evolution of Fe-S bond properties with pressure. J. Geophys. Res. 113, B10205. https://doi.org/10.1029/2008JB005663.

Morgan, J.W., Anders, E., 1980. Chemical composition of Earth, Venus, and Mercury. Proc. Natl. Acad. Sci. 77, 6973–6977. https://doi.org/10.1073/pnas.77.12.6973.

Namur, O., Charlier, B., 2017. Silicate mineralogy at the surface of Mercury. Nat. Geosci. 10, 9–13. https://doi.org/10.1038/ngeo2860.

Namur, O., Charlier, B., Holtz, F., Cartier, C., McCammon, C., 2016. Sulfur solubility in reduced mafic silicate melts: implications for the speciation and distribution of sulfur on Mercury. Earth Planet. Sci. Lett. 448, 102–114. https://doi.org/10.1016/j.epsl.2016.05.024.

Nittler, L.R., Starr, R.D., Weider, S.Z., McCoy, T.J., Boynton, W.V., Ebel, D.S., Ernst, C.M., Evans, L.G., Goldsten, J.O., Hamara, D.K., Lawrence, D.J., McNutt, R.L., Schlemm, C.E., Solomon, S.C., Sprague, A.L., 2011. The major-element composition of Mercury's surface from MESSENGER X-ray spectrometry. Science 333, 1847–1850. https://doi.org/10.1126/science.1211567.

Nittler, L.R., Weider, S.Z., 2019. The surface composition of Mercury. Elements 15, 33–38. https://doi.org/10.2138/gselements.15.1.33.

Poirier, J.-P., 1994. Light elements in the Earth's outer core: a critical review. Phys. Earth Planet. Inter. 85, 319–337. https://doi.org/10.1016/0031-9201(94)90120-1.

Sanloup, C., Fei, Y., 2004. Closure of the Fe–S–Si liquid miscibility gap at high pressure. Phys. Earth Planet. Inter. 147, 57–65. https://doi.org/10.1016/j.pepi.2004.06.008.

Smith, D.E., Zuber, M.T., Phillips, R.J., Solomon, S.C., Hauck, S.A., Lemoine, F.G., Mazarico, E., Neumann, G.A., Peale, S.J., Margot, J.-L., Johnson, C.L., Torrence, M.H., Perry, M.E., Rowlands, D.D., Goossens, S., Head, J.W., Taylor, A.H., 2012. Gravity field and internal structure of Mercury from MESSENGER. Science 336, 214–217. https://doi.org/10.1126/science.1218809.

Smith, D.E., Zuber, M.T., Phillips, R.J., Solomon, S.C., Neumann, G.A., Lemoine, F.G., Peale, S.J., Margot, J.-L., Torrence, M.H., Talpe, M.J., Head, J.W., Hauck, S.A., Johnson, C.L., Perry, M.E., Barnouin, O.S., McNutt, R.L., Oberst, J., 2010. The equatorial shape and gravity field of Mercury from MESSENGER flybys 1 and 2. Icarus 209, 88–100. https://doi.org/10.1016/j.icarus.2010.04.007.

Solomon, S.C., Byrne, P.K., 2019. The exploration of Mercury by spacecraft. Elements 15, 15–20. https://doi.org/10.2138/gselements.15.1.15.

Tateno, S., Hirose, K., Sinmyo, R., Morard, G., Hirao, N., Ohishi, Y., 2018. Melting experiments on Fe–Si–S alloys to core pressures: silicon in the core? Am. Mineral. 103, 742–748. https://doi.org/10.2138/am-2018-6299.

Tateno, S., Kuwayama, Y., Hirose, K., Ohishi, Y., 2015. The structure of Fe–Si alloy in Earth's inner core. Earth Planet. Sci. Lett. 418, 11–19. https://doi.org/10.1016/j.epsl.2015.02.008.

Wade, J., Wood, B.J., 2005. Core formation and the oxidation state of the Earth. Earth Planet. Sci. Lett. 236, 78–95. https://doi.org/10.1016/j.epsl.2005.05.017.

Zolotov, M.Yu., Sprague, A.L., Hauck, S.A., Nittler, L.R., Solomon, S.C., Weider, S.Z., 2013. The redox state, FeO content, and origin of sulfur-rich magmas on Mercury. J. Geophys. Res., Planets 118, 138–146. https://doi.org/10.1029/2012JE004274.

Zuber, M.T., Smith, D.E., Phillips, R.J., Solomon, S.C., Neumann, G.A., Hauck, S.A., Peale, S.J., Barnouin, O.S., Head, J.W., Johnson, C.L., Lemoine, F.G., Mazarico, E., Sun, X., Torrence, M.H., Freed, A.M., Klimczak, C., Margot, J.-L., Oberst, J., Perry, M.E., McNutt, R.L., Balcerski, J.A., Michel, N., Talpe, M.J., Yang, D., 2012. Topography of the northern hemisphere of Mercury from MESSENGER laser altimetry. Science 336, 217–220. https://doi.org/10.1126/science.1218805.